COMMUNICATION

Check for updates

Gradient-structured directional porous floatable aerogels for effective solar-driven hydrogen production and steam generation

Changsong Shi,†[a] Rongtao Zheng, [iD] †[b] Yihe Yue,[a] Mingliang Wu,[c] Pengfei Li,[a] Linfeng Fan,[c] Chi Guo,[a] Xin Zhang,[a] Peiyu Luo,[a] Jiawen Zhang, [iD] [d] Cuilian Wen, [iD] [b] Jinlan Wang, [iD] *[c] Baisheng Sa [iD] *[b] and Zhiyang Lyu [iD] *[a]

Solar-driven reaction technology offers a promising route to clean energy generation and sustainable development. Despite significant advancements in photocatalysts and photothermal materials, challenges remain in device structural design, including insufficient light utilization, slow water transport, and inefficient gas separation. Here, we design a floatable cellulose nanofiber aerogel featuring a gradient-structured directional porous architecture to address these challenges. The designed aerogel integrates multiple structural features, including a bottom layer with large directional channels for rapid water transport, a top functional floatable layer with small directional channels for enhanced gas separation and active material loading, and a micron-scale embossed surface structure to maximize light utilization. As a result, the photocatalytic aerogels achieved a high hydrogen generation rate of 60.7 mmol m^{-2} h^{-1}, significantly outperforming the conventional thin-film photocatalytic platforms. Meanwhile, the photothermal aerogels exhibited a high water evaporation rate of 1.62 kg m^{-2} h^{-1} with excellent salt-resistance capability, and a high freshwater collection rate of 1.65 mL m^{-2} h^{-1} under outdoor field-scale conditions. This study demonstrates a novel and scalable strategy for developing high-efficiency solar-driven reaction platforms, with strong potential for future industrial applications.

New concepts

We report a novel structural design of solar-driven reaction platforms by developing a floatable cellulose nanofiber aerogel with a gradient-structured directional porous architecture. This multifunctional aerogel uniquely integrates large bottom channels for rapid water transport, small top-layer channels for efficient gas separation and active material loading, and a micron-scale embossed surface for enhanced light harvesting. Unlike conventional flat thin-film photocatalytic systems, which typically suffer from poor water management and limited light utilization, our design offers a synergistic improvement in mass transport, light absorption, and spatial separation of gas and liquid phases. This innovation leads to a significantly enhanced photocatalytic hydrogen evolution rate and photothermal water evaporation efficiency, demonstrating superior performance under both laboratory and outdoor field-scale conditions. Our work introduces a new paradigm in materials design—one that merges structural anisotropy, functional layering, and surface microstructuring to address multiple bottlenecks in solar energy conversion. Beyond performance enhancement, this aerogel platform is scalable, light weight, and derived from renewable materials, offering strong potential for real-world applications in off-grid hydrogen generation and clean water production. This study provides new insights into how architecture-driven design can unlock the full potential of advanced materials in sustainable energy and environmental technologies.

1. Introduction

Solar-driven reaction technologies have shown considerable promise in diverse applications, such as photocatalytic hydrogen (H$_2$) production,[1–3] photothermal desalination,[4–6] and environmental pollution remediation,[7–9] owing to their high solar energy utilization efficiency, environmental sustainability, and operational simplicity.[10–12] Among them, photocatalytic H$_2$ production is particularly noteworthy as a key approach for generating green H$_2$, an essential component of future sustainable energy systems.[13,14] The efficiency of this process is primarily governed by the catalytic activity of the photocatalyst.[15,16] Over the past decade, various semiconductor photocatalysts have been developed to enhance photocatalytic performance, such as metal oxides (*e.g.*, TiO$_2$),[17,18] metal sulfides (*e.g.*, CdS),[19,20] perovskites,[21,22] covalent organic frameworks (COFs, *e.g.*, covalent triazine framework (CTF)),[23,24] and graphitic carbon nitride (g-C$_3$N$_4$).[25,26] While these materials have demonstrated significant progress in improving light

[a] *School of Mechanical Engineering, Jiangsu Key Laboratory for Design and Manufacturing of Precision Medicine Equipment, Southeast University, Nanjing, 211189, China. E-mail: zhiyanglyu@seu.edu.cn*

[b] *College of Materials Science and Engineering, Fuzhou University, Fuzhou, 350108, China. E-mail: bssa@fzu.edu.cn*

[c] *School of Physics, Key Laboratory of Quantum Materials and Devices of Ministry of Education, Southeast University, Nanjing, 211189, China. E-mail: jlwang@seu.edu.cn*

[d] *School of Materials Science and Engineering, Jiangsu Key Laboratory of Construction Materials, Southeast University, Nanjing, 211189, China*

† These authors contributed equally to this work.

absorption, suppressing recombination of photogenerated charge carriers, and enhancing chemical stability, they are typically used in powder form dispersed in water. This configuration limits their performance due to diminished light absorption under submerged test conditions.[27,28] Moreover, the inefficient separation of the generated H_2 gas at the catalyst surface further constrains the overall reaction efficiency.[29] To overcome these limitations, various multiphase reaction system designs have been proposed, including particulate sheet,[30] film,[31,32] and flat sheet configurations.[33] While these systems have demonstrated notable enhancements in photocatalytic performance, significant challenges remain in uniform photocatalyst dispersion, efficient mass transfer, and rapid product separation.

In recent years, aerogels have emerged as promising candidates for enhancing the efficiency of solar-driven reactions, owing to their high porosity, low density, and large specific surface area.[34,35] Their unique porous architectures, excellent floatability, and exceptional optical properties contribute to optimized light absorption and reflection, thereby minimizing energy loss and maximizing solar energy utilization.[36–38] Recent studies have explored a variety of aerogel structures for photothermal desalination,[39–41] including macroscopic light-trapping designs to improve light absorption,[42,43] directional channels to accelerate water transport,[44,45] 3D hierarchical porous structures to facilitate gas separation,[46,47] and floatable configurations to ensure environmental adaptability.[48,49] These floatable structural innovations offer valuable guidance for designing efficient photocatalytic H_2 production systems. In addition, most existing studies have focused on single-scale pore structures or single-functionality designs, limiting the potential for multifunctional integration. Therefore, the development of advanced multiscale porous aerogels that can simultaneously address multiple functional requirements is urgently needed, with significant implications for practical deployment in solar-driven reaction technologies.

In this study, we designed and developed a novel floatable cellulose nanofiber (CNF)-based aerogel featuring gradient-directional porous channels, serving as a multifunctional platform for photocatalytic H_2 production and photothermal steam generation applications. The designed aerogel integrates multiple structural features, including a bottom layer with large directional channels for rapid water transport, a top functional floatable layer with small directional channels for enhanced gas separation and active material loading, and a micron-scale embossed surface structure to maximize light utilization. This floating gradient-structural synergy enables simultaneous enhancement of light absorption, mass transfer, and phase separation in solar-driven interfacial reactions. Benefiting from this integrated design, the photocatalytic aerogel achieved a high hydrogen generation rate of 60.7 mmol m^{-2} h^{-1}, significantly outperforming conventional thin-film photocatalytic platforms, while the photothermal aerogels demonstrated a high water evaporation rate of 1.62 kg m^{-2} h^{-1} with excellent salt-resistance capability, and a rapid freshwater collection rate of 1.65 mL m^{-2} h^{-1} in an outdoor field-scale evaporation and condensate collection system. This study provides a scalable and practical strategy for the design of high-performance solar-driven reaction platforms, showing great potential for industrial-scale applications.

2. Results and discussion

2.1 Design and fabrication of gradient-structured directional porous floatable aerogels

Fig. 1a illustrates the conceptual design and advantages of the gradient-structured directional porous floatable aerogels developed as platforms for solar-driven H_2 production and steam generation applications. In contrast to traditional planar films or isotropic aerogels, our floating gradient-structured aerogel enables simultaneous resolution of three critical challenges in solar-driven interfacial reaction, including light absorption, mass transfer, and phase separation. Specifically, the bottom layer serves as the water-transport layer, featuring large directional channels formed from a low-concentration CNF solution to facilitate efficient water delivery to the reaction site. The top functional layer consists of small directional channels, fabricated from a high-concentration CNF solution to enhance gas separation and support the high loading of active materials. To further optimize light utilization, a micron-scale embossed structure is fabricated on the top layer to enhance light reflection and increase solar energy absorption. Moreover, the floatability of the aerogels allows for direct exposure of the functional layer to incident light, effectively addressing challenges related to low light transmission efficiency and poor gas separation. In this design, the gradient structure not only synergistically improves the transport of reactant water and product gas within the channels but also enables highly efficient solar-driven reactions. To validate the design, COMSOL Multiphysics simulations were performed to compare water transport behaviors in aerogels with disordered, large directional-channel, and small-channel structures (Fig. 1b). The simulation results revealed that disordered channels exhibited the slowest water transport due to high diffusion resistance and tortuous pathways, consistent with previous reports.[50] In contrast, aerogels with large channels demonstrated superior water transport performance, attributed to their minimized flow resistance, outperforming those with small channel configurations.

Fig. 2a shows the fabrication process of gradient-structured directional porous aerogels using a well-established freeze-casting strategy. Firstly, the dilute CNF solution and concentrated CNF solution (containing the active material) were separately stirred with a defoamer to form homogeneous precursor mixtures for each layer. The structure was then assembled using a layer-by-layer directional freezing process. The dilute CNF solution was slowly deposited onto a copper plate at -20 °C, forming large directional channels in the bottom layer for rapid water transport. Next, the concentrated CNF solution was coated onto the upper layer to form the functional layer. To enhance light absorption, a micron-scale embossed pore structure was created on the surface of the top layer using 3D-printed molds, which were tightly bonded to
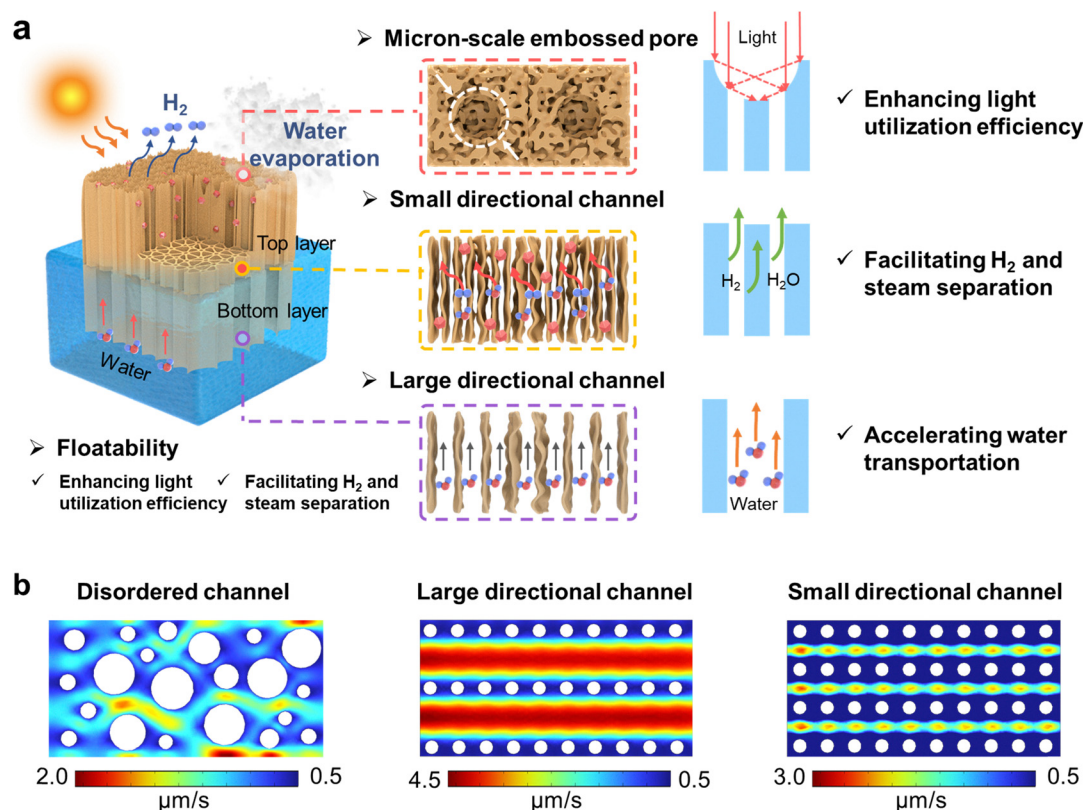
Fig. 1 Conceptual design and advantages of gradient-structured directional porous floatable aerogels for solar-driven reactions. (a) Schematic illustration of the design concept. (b) COMSOL multiphysics simulation of water transport rates within the disordered, large directional-channel, and small-channel structures. White regions represent solid barriers, while the colored background indicates the velocity distribution of water flow through the channels. As shown in the color bar, blue corresponds to low flow velocity and red to high flow velocity.

ensure a directional gradient pore structure (Fig. S1). Finally, the gradient-structured directional porous floatable aerogels were obtained through freeze drying. During freezing, the advancing ice front directionally expelled the suspended solutes (including CNFs and functional additives) into the intercrystalline regions. Subsequent freeze-drying removed the ice *via* sublimation, yielding vertically aligned porous channels templated by directional ice growth.
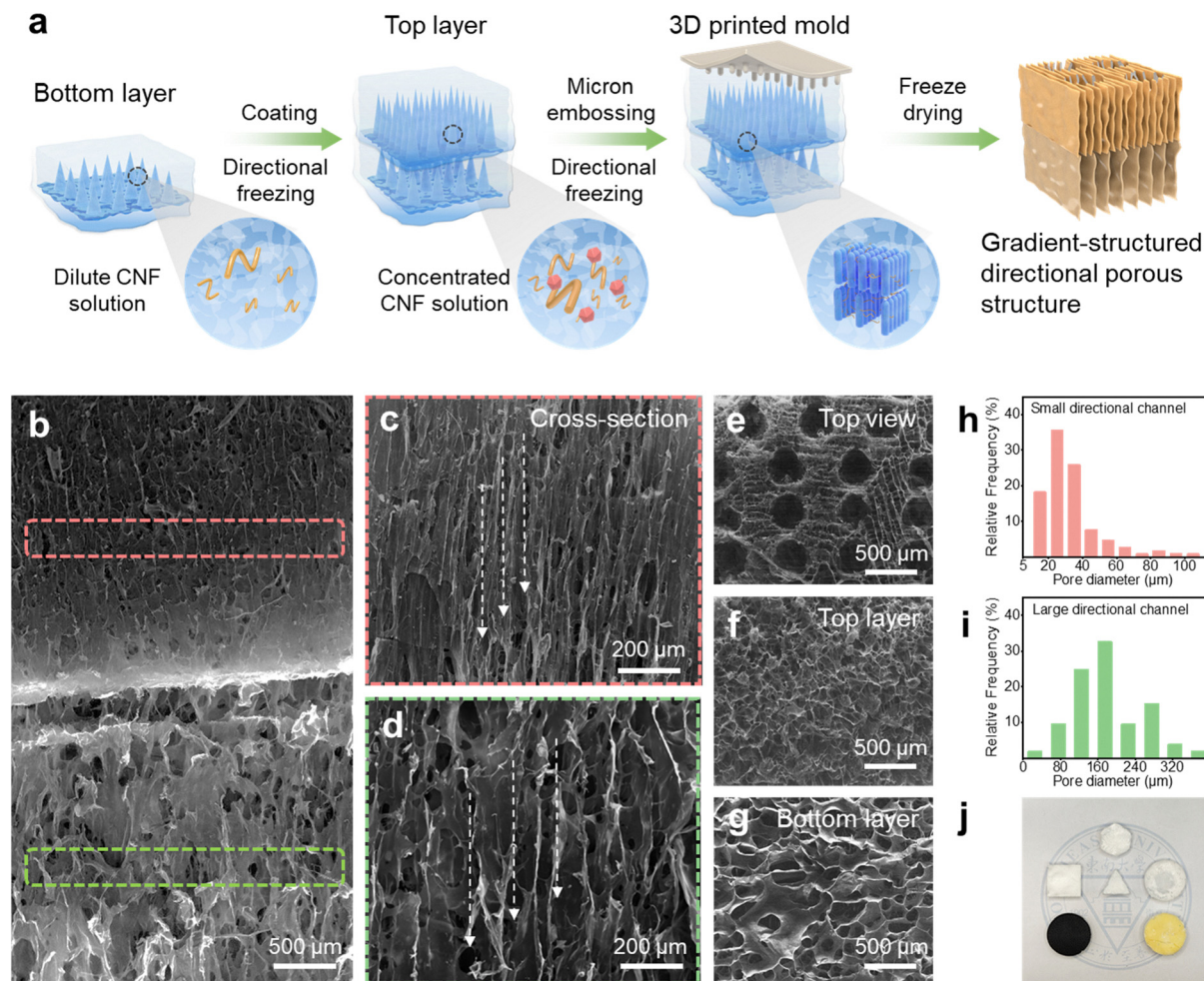
The morphology of the gradient-structured aerogels was characterized using scanning electron microscopy (SEM). Fig. 2b reveals the distinct pore orientation, stratification, and a well-defined contact interface between layers. During the initial stage of the directional freezing process, ice crystals compressed the precursors, causing their accumulation at the bottom and forming a dense aerogel pore wall. The clearly different pore-size channels demonstrated the formation of a gradient pore structure (Fig. 2c and d). The surface morphology of each layer was further analyzed, as shown in Fig. 2e–g, also demonstrating discontinuous variations in pore size. These structural differences were controlled by adjusting the ice crystal growth direction and CNF concentration (Fig. S2). The pore size of each layer was subsequently measured, indicating an average pore size of ~ 30 μm in the small directional-pore functional layer (Fig. 2f and h) and ~ 150 μm in the large directional-pore water transport layer (Fig. 2g, i and Fig. S3). The orientation histograms show that the small directional channels

exhibit a sharp peak centered at 90°, while the large directional channels display a broader distribution centered around 75°, indicating a high level of structural alignment (Fig. S4). Additionally, Fig. 2j highlights the customizable design of the gradient-structured directional porous aerogels for customized solar-driven reaction devices.

2.2 Properties of gradient-structured directional porous floatable aerogels

Fig. 3 presents the physicochemical and mechanical properties of the obtained gradient-structured directional porous aerogels. As shown in Fig. 3a, the aerogels are remarkably lightweight, as evidenced by their ability to rest on a dandelion. This ultralight property was quantitatively supported by the exceptionally low density of the CNF-based aerogels, measured at 0.0139 g cm^{-3}, significantly lower than that of chitosan (CS)-based aerogels $(0.0182$ g cm$^{-3})$ and polyvinyl alcohol (PVA)-based aerogels $(0.2673$ g cm$^{-3})$ fabricated under identical conditions (Fig. 3b and Fig. S5). This low density contributes significantly to the excellent floatability of aerogels. Efficient water transport is essential for both photocatalytic H$_2$ production and photothermal desalination, as aerogels must continuously absorb and deliver water to the top functional layer to sustain solar-driven reactions. To evaluate water transport efficiency, aerogels with large and small directional channels were fabricated for

Fig. 2 Fabrication and morphological characterization of gradient-structured directional porous aerogels. (a) Schematic illustration of the fabrication process, including directional-freezing coating, micron embossing, and freeze-drying. (b) SEM images of cross-sections showing the entire gradient aerogels. (c) and (d) Enlarged cross-section SEM images of the top layer (c) and the bottom layer (d). (e)–(g) Surface SEM images of micron-scale embossed pores (e), small directional channels (f), and large directional channels (g). (h) and (i) Pore size distribution analysis of the top and bottom layers. (j) Digital photographs of customized shapes of aerogels.

comparison under the same experimental conditions. As shown in Fig. 3c, aerogels with large directional channels exhibited significantly faster water absorption capability compared to their small-channel counterparts. This enhanced transport performance is attributed to the reduced hydraulic resistance of the larger channels, which facilitates bulk water flow governed by Darcy's law rather than capillary-driven transport.[51] Although small pores support capillary rise, their contribution becomes negligible at the micrometer scale considered here. Consequently, the large-channel aerogels were designated as the bottom layer to facilitate rapid and continuous water transport, especially under high-throughput solar-driven evaporation.

The floatability of the functional layer is a crucial property in photocatalytic systems, as it ensures efficient light exposure and facilitates gas separation during solar-driven reactions. To evaluate this property, three low-density aerogels with different compositions were evaluated. As shown in Fig. 3d–f, CNF-based aerogels demonstrated excellent floatability and recyclability over a one-week testing period. In contrast, PVA-based aerogels

exhibited poor floatability due to their high hydrophilicity and swelling behavior. Upon water absorption, the hydrogen bonds between PVA molecule chains were disrupted, increasing molecular chain distance and ultimately raising the density, causing it to sink.[52] Similarly, CS aerogels absorbed significant amounts of water due to the abundance of hydrophilic functional groups ($-NH_2$ and $-OH$),[53] which compromised their structural integrity. After a seven-day recycling test, the CNF aerogels maintained structural stability, with a minimal weight loss of only 2.9% and negligible material leaching, demonstrating excellent long-term floatability (Fig. 3e and f and Fig. S6). To further investigate the effect of the micron-scale embossed structure on optical performance, UV-visible diffuse reflectance spectra were measured before and after embossing. As shown in Fig. 3g, the embossed aerogels exhibited an extended visible light absorption range due to enhanced light scattering and multiple internal reflections, indicating enhanced absorption efficiency across the visible spectrum.

We then investigated the influence of directional porous channels of the obtained aerogels on their compressive properties
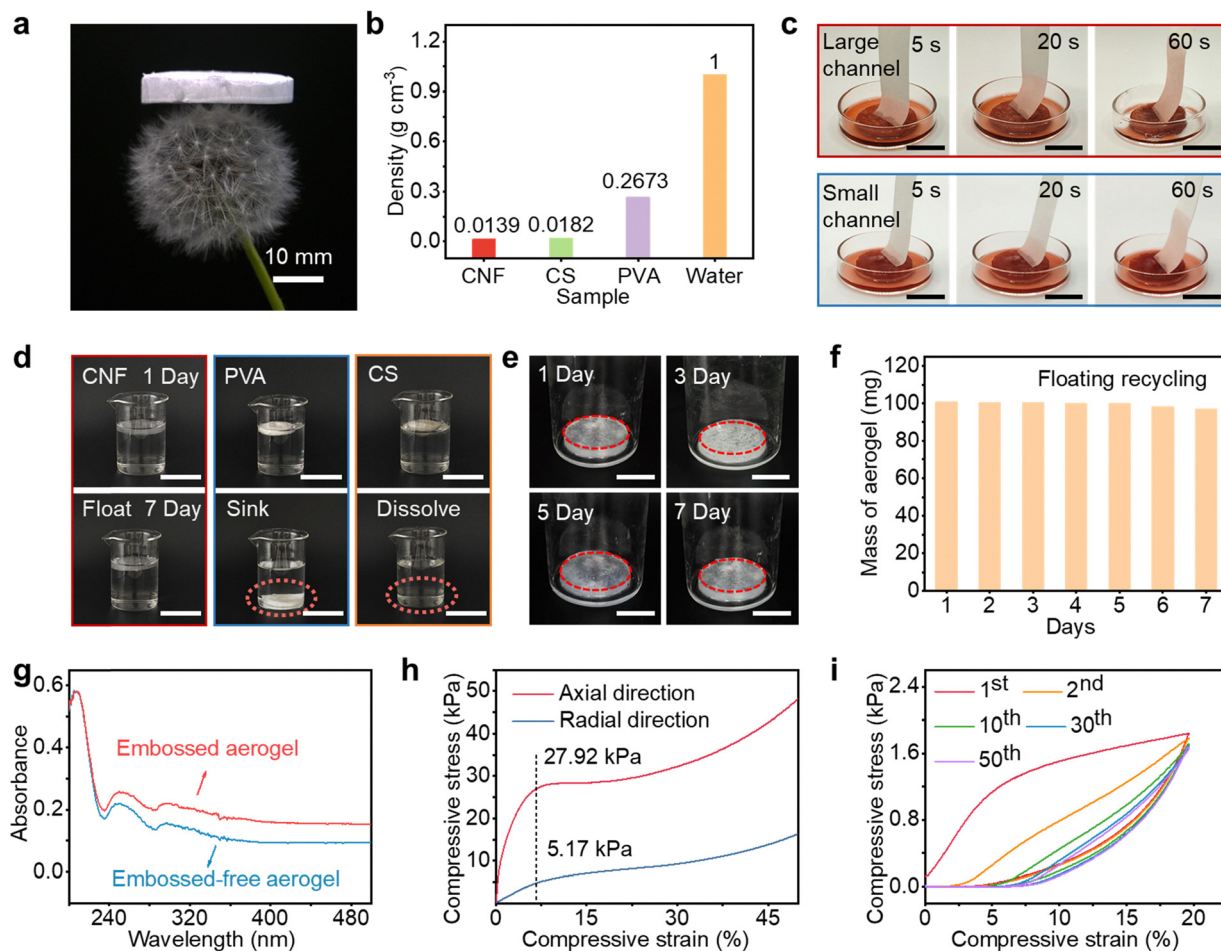
Fig. 3 Properties of gradient-structured directional porous floatable aerogels. (a) Digital image of the lightweight properties of CNF-based aerogels. (b) Densities of different aerogels. (c) Water transportation capacity comparison among different aerogel structures. The scale bars are 2 cm. (d) Floatability test. The scale bars are 4 cm. (e) and (f) Recycling performance of CNF-based aerogels over a seven-day testing period. The scale bars are 2 cm. (g) UV-visible spectra of the aerogels before and after embossing. (h) Compressive stress–strain curves of the aerogels in the axial direction and radial direction. (i) Stress–strain curves compressed in radial directions under 20% strain for 50 loading–unloading cycles.

along both axial and radial directions. As shown in Fig. 3h, the axial compressive stress reached 27.92 kPa at ∼7% strain, which was significantly higher than that of the radial direction stress of 5.17 kPa at the same strain level. This pronounced difference was attributed to the unique directional pore structure, which exhibited strong anisotropy, resulting in higher compressive stress under the same strain.[54,55] To further assess the durability of the aerogels, 50 cycles of loading–unloading compression tests were performed along the radial direction at 20% strain (Fig. 3i). The aerogels exhibited only a slight reduction in both stress and strain retention, demonstrating excellent reversible compressibility and outstanding fatigue resistance. These mechanical properties highlight their potential for long-term cyclic use in solar-driven reaction devices or other environments subject to repeated mechanical deformation.

2.3 Photocatalytic H_2 production performance of the gradient-structured floatable aerogels

As schematically illustrated in Fig. 4a, the photocatalytic H_2 production performance of the structural aerogels was

evaluated using a custom-designed solar-driven reaction setup. The photocatalyst was selectively incorporated into the top functional layer of the aerogel (Fig. 4b and Fig. S7). The selected biphenyl-based covalent triazine framework (CTF-BIP) photocatalyst was previously identified and optimized through machine-learning screening in our earlier studies.[56,57] It exhibited excellent structural stability under visible-light irradiation, and its molecular design prevents hydrogen release *via* self-decomposition, confirming that the observed hydrogen evolution originates from photocatalytic activity rather than catalyst degradation. Detailed preparation methods and characterization are provided in Fig. S8–S10. To highlight the optical advantages introduced by the embossed gradient directional pore structure, we fabricated control aerogels without a micron-scale embossed pore structure and with only large directional channels. As shown in Fig. S11, the embossed gradient aerogels exhibited broader visible light absorption than the aerogels without an embossed pore structure, which was attributed to the micron-scale embossed pore structure enhancing light utilization through multiple internal reflections.
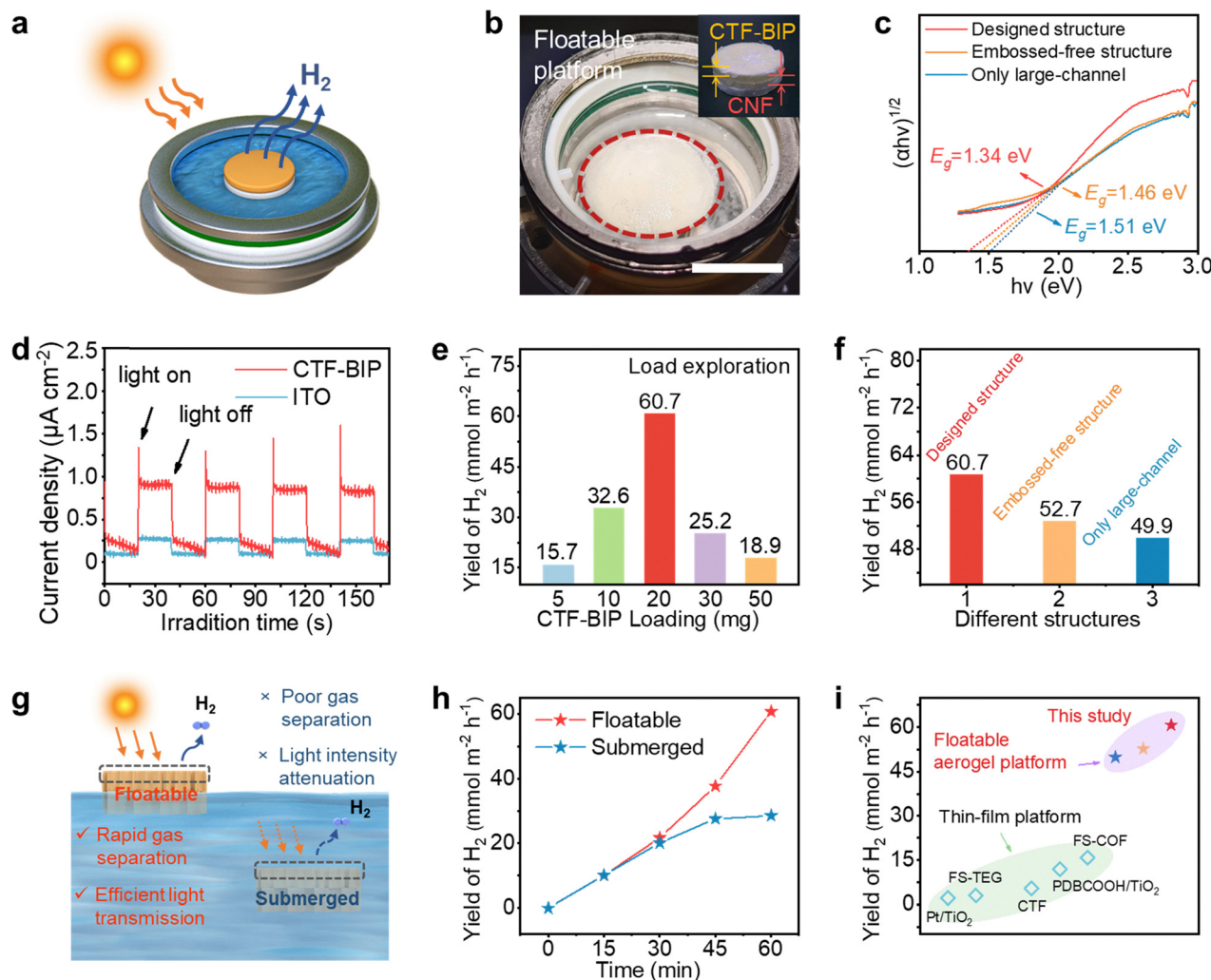
Fig. 4 Photocatalytic H$_2$ production performance of the gradient-structured floatable aerogels integrated with the CTF–BIP photocatalyst. (a) Schematic illustration of the photocatalytic reaction setup. (b) Photograph of the floatable platform during the photocatalytic experiment, the upper right corner is the photograph of the floatable platform. The scale bar is 20 mm. (c) Tauc plots of aerogels with the designed, embossed-free, and only large-channel structures, derived from UV-vis data (Fig. S10), showing $(\alpha h\nu)^{1/2}$ *versus* hν for bandgap estimation. (d) Transient photocurrent response curves under light on−off cycles. (e) H$_2$ production performances of aerogels with varying CTF–BIP loading. (f) Comparison of H$_2$ production efficiency among different structural designs. (g) Schematic of the photocatalytic H$_2$ production experiment using floatable and submerged states. (h) H$_2$ generation rates of aerogels in floatable *versus* submerged states. (i) Benchmark comparison of the H$_2$ production rates with reported state-of-the-art thin-film photocatalytic platforms, including Pt/TiO$_2$ film,[58] FS-TEG film (a fluorene-dibenzo[*b,d*]thiophene sulfone side chain substituted with triethylene glycol side chains);[59] FS-COF film (a benzobis (benzothiophene sulfone) based COF);[60] CTF-film;[61] and PDBCOOH (a donor−acceptor type conjugated organic polymer with *n*-butyric acid group).[62]

In addition, the aerogels lacking the gradient features displayed a similar absorption across the visible spectrum. Bandgap (E_g) estimation using Tauc plots showed a clear reduction in the optical bandgap, from 1.51 to 1.34 eV, upon the introduction of gradient and imprinted structures (Fig. 4c). The narrow bandgap enables efficient visible-light harvesting, thereby enhancing photocatalytic H$_2$ production. As shown in Fig. 4d, transient photocurrent response measurements further validated the superior charge carrier dynamics of the CTF-BIP-based aerogels. The electrodes demonstrated a rapid and stable photocurrent response during repeated on−off light cycles, indicative of effective photoinduced charge separation.

To optimize catalytic performance, different CTF-BIP loading amounts were tested. As shown in Fig. 4e, the maximum hydrogen yield of 60.7 mmol m^{-2} h^{-1} was obtained at a loading of 20 mg. Beyond this threshold, photocatalytic efficiency declined due to the aggregation of CTF particles, which reduced the surface-active area. A blank control using a pure CNF-based gradient aerogel (without CTF-BIP) was also tested and showed a negligible H$_2$ generation rate of only 1.2 mmol m^{-2} h^{-1}, confirming the critical role of CTF-BIP in driving the photocatalytic reaction (Fig. S11). Fig. 4f shows the comparison of H$_2$ evolution yield for the aerogels with different structures. The aerogel with a directional gradient pore structure achieved the highest H$_2$ generation rate of 60.7 mmol m^{-2} h^{-1},

outperforming control samples with only large directional channels (49.9 mmol m^{-2} h^{-1}) and embossed-free pore structure (52.7 mmol m^{-2} h^{-1}), consistent with their respective light absorption capacity (Fig. S12). To assess the long-term stability, repeated hydrogen evolution tests were conducted over six consecutive cycles under identical conditions (Fig. S13). The CTF-BIP-loaded gradient aerogel retained over 93.5% of its initial activity, with hydrogen production decreasing only slightly from 60.7 to 56.8 mmol m^{-2} h^{-1}, demonstrating excellent fatigue resistance and photocatalytic durability.

As shown in Fig. 4g, the floatable aerogel platform exhibited superior light absorption and rapid gas separation capabilities compared to the submerged aerogel counterpart. To further investigate the effect of floatability, a comparison was made between floatable and submerged photocatalyst platforms. As shown in Fig. 4h, the floatable aerogels achieved a twofold improvement in the H$_2$ generation rate, reaching 60.7 mmol m^{-2} h^{-1}, significantly surpassing the submerged samples (28.6 mmol m^{-2} h^{-1}). This enhancement is attributed to the initial establishment of thermal equilibrium and directional water transport, followed by sustained heat localization and efficient mass transfer, as reported in related studies.[63] These results highlight the importance of the embossed gradient directional pore structure and floation in maximizing light exposure and gas diffusion during photocatalysis.

More importantly, our designed aerogel-based photocatalytic platform demonstrates a much higher H$_2$ production rate than many reported state-of-the-art traditional thin-film photocatalytic platforms (Fig. 4i), which are often challenging to fabricate and scale. Additionally, the performance surpasses that of previously reported aerogel-based platforms, including the photocatalytic system consisting of directional pore-structured carbonized wood (39.98 mmol m^{-2} h^{-1})[64] and photothermal–photocatalytic layered aerogels (17.94 mmol m^{-2} h^{-1}),[65] although it remains slightly lower than the most recent advanced designs (163 mmol m^{-2} h^{-1}).[63] Nevertheless, with further optimization of the photocatalytic materials, there is substantial potential to significantly enhance the overall efficiency of the platform.

2.4 Photothermal steam generation performance of the gradient-structured aerogels

As illustrated in Fig. 5a, we further evaluated the photothermal steam generation performance of the gradient-structured aerogel, in which a photothermal material was integrated into the top functional layer. The photothermal material used was a 2D MXene/reduced graphene oxide (r-GO) composite (Fig. 5b), known for its excellent light-to-heat conversion efficiency.[66] The detailed preparation processes and characterization results
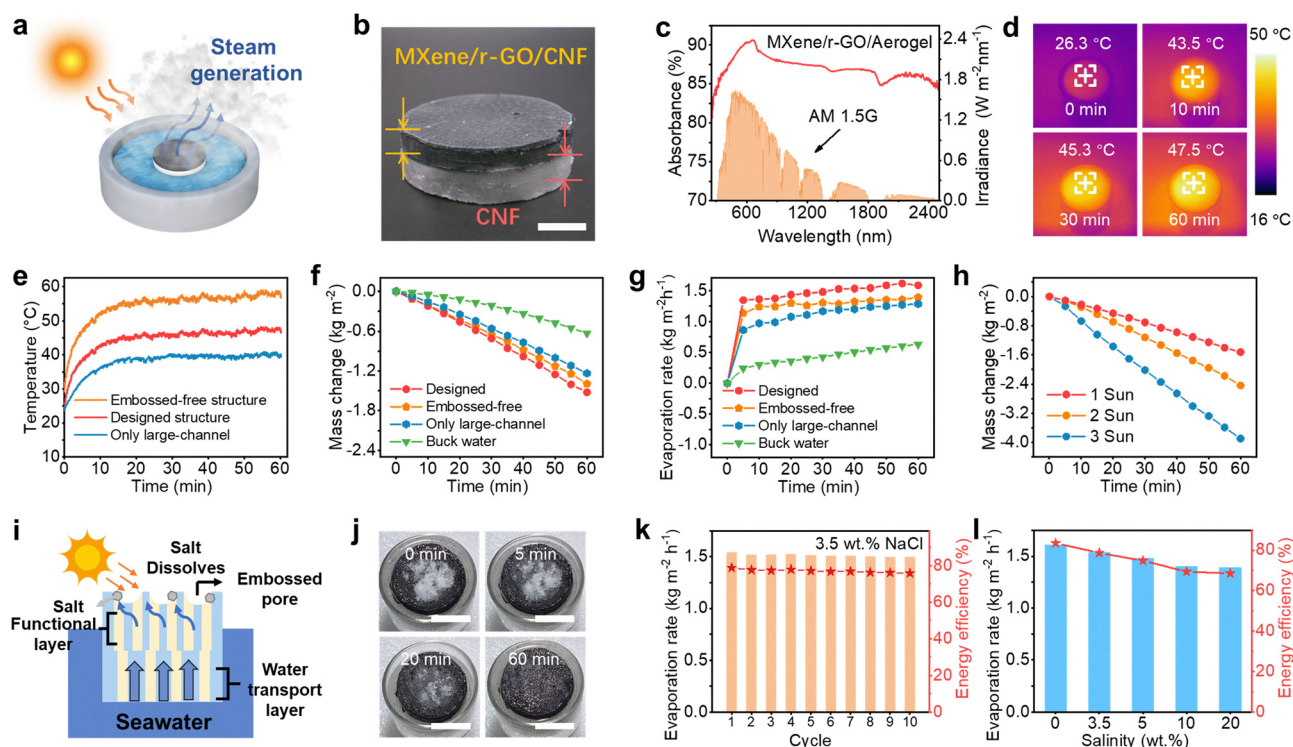

Fig. 5 Photothermal steam generation performance of the gradient-structured aerogels integrated with the MXene/r-GO photothermal materials. (a) Schematic illustration of the experimental setup for photothermal steam generation. (b) Photograph of the gradient-structured photothermal aerogels. The scale bar is 10 mm. (c) UV-vis-NIR diffuse reflectance spectra. (d) Infrared thermal images under 1 Sun irradiation within 1 hour. (e)–(g) Comparison of surface temperature change evolutions (e), evaporated water mass changes (f), and evaporation rates (g) for different structural designs. (h) Evaporated water mass changes under irradiation from 1 to 3 Suns. (i) and (j) Schematic illustration and experimental demonstration of salt-resistance capability. The scale bars are 20 mm. (k) and (l) Evaporation rates and corresponding solar-to-vapor energy efficiencies in (k) 3.5 wt% NaCl solution and (l) NaCl solutions with varying concentrations.

are provided in Fig. S14–S16. A key factor influencing solar vapor generation is the light absorption capability of the photothermal material. As shown in Fig. 5c, the gradient-structured aerogel exhibited strong broadband light absorption, achieving an average absorbance of approximately 90% across the 250 to 2500 nm wavelength range. This high absorbance ensures efficient photothermal conversion under solar irradiation. To validate the enhanced photothermal properties conferred by the gradient-structured directional porous architecture, aerogels with different structural configurations were fabricated as control samples, similar to those used in photocatalytic testing. As shown in Fig. 5d and e and Fig. S17, the embossed gradient porous aerogel achieved a steady-state surface temperature of 47.5 °C within 20 min under simulated solar illumination. In contrast, aerogels lacking either the gradient or the embossed features reached steady-state surface temperatures of 38.7 and 59.7 °C, respectively. The observed differences in thermal performance are likely due to the inability of non-gradient structures to effectively balance water transport with evaporation (Fig. S18). The embossed gradient structure, in contrast, facilitates directional water delivery from the bulk reservoir to the heated surface while maintaining high evaporation rates, resulting in more efficient and sustainable photothermal steam generation.

Fig. 5f and g present the water mass loss and corresponding evaporation rates for different structures and bulk water over

1 hour under 1 Sun irradiation. The embossed gradient porous aerogel achieved a high evaporation rate of 1.62 kg m^{-2} h^{-1}, significantly outperforming the embossed-free gradient structure of 1.35 and the large directional channels of 1.28 kg m^{-2} h^{-1}. This performance improvement highlights the synergistic benefit of combining vertical gradient channels with surface embossing to enhance photothermal-driven water evaporation. The pure CNF gradient aerogel without photothermal materials exhibited a low evaporation rate of 0.43 kg m^{-2} h^{-1}, confirming that the improved performance primarily arises from the photothermal component (Fig. S19). Further analysis of Fig. 5h and Fig. S20 shows the dependence of the evaporation rate on light intensity. Under increasing solar intensities up to 3 Suns, the evaporation rate of the embossed gradient porous structure increased nearly linearly, achieving approximately a 2.5-fold enhancement compared to 1 Sun irradiation, demonstrating excellent scalability and responsiveness under intensified solar conditions.

The embossed gradient porous aerogel also exhibited outstanding salt resistance, as schematically shown in Fig. 5i. Even after extended operation under saline conditions, no significant salt crystallization was observed on the aerogel surface (Fig. 5j). In contrast, aerogels with either an embossed-free structure or disordered pore structure showed clear signs of salt accumulation (Fig. S21). This superior anti-fouling performance is attributed to the synergistic effect of the vertical gradient channels and micron-scale embossed surface, which together facilitate
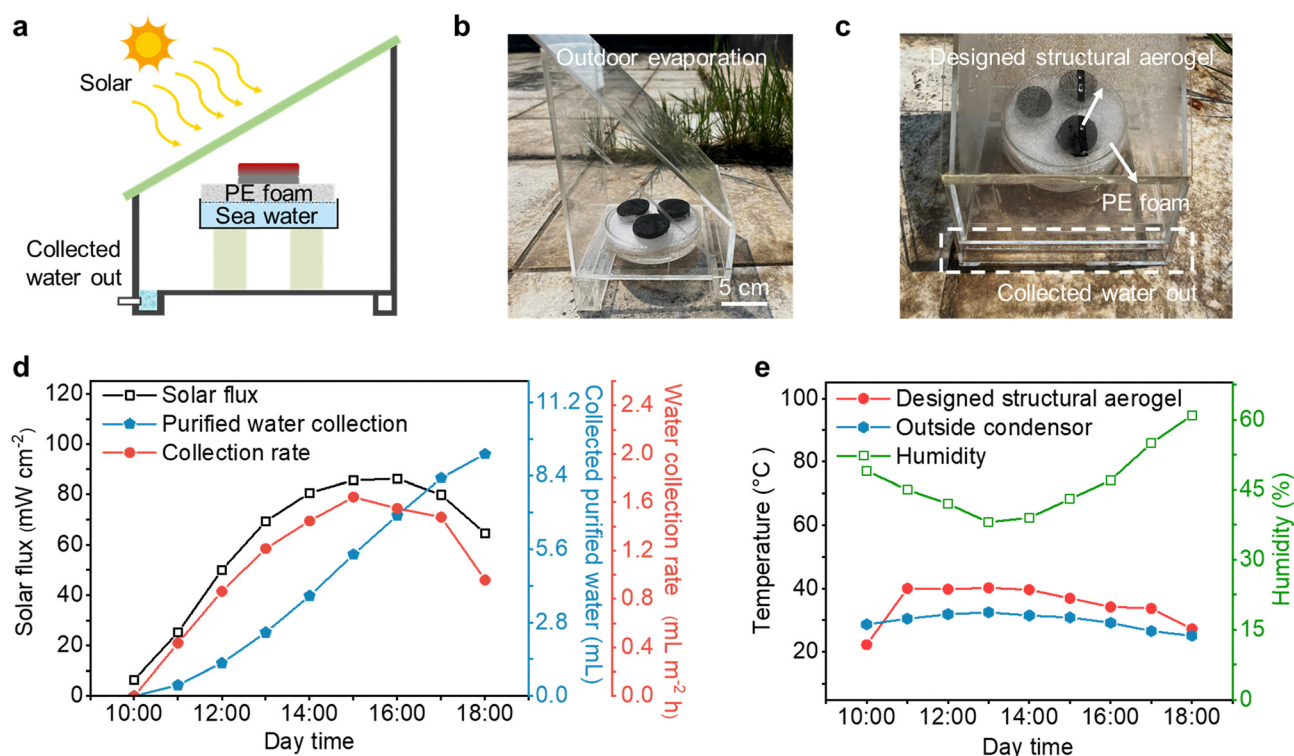
Fig. 6 Photothermal desalination performance of the outdoor solar desalination system. (a)–(c) Conceptual design and corresponding photographs of the solar desalination system for saline water purification. (d) Temporal variations of solar flux, water collection rate, and cumulative yield of purified water during the outdoor test period. (e) Monitored changes in temperature and humidity inside and outside the solar desalination system throughout the test duration.

continuous upward water transport and promote ion back-diffusion, thereby preventing local salt accumulation. Moreover, the embossed surface promotes vapor escape, further mitigating the risk of salt precipitation.[67] As shown in Fig. 5k, the evaporation rates and solar energy conversion efficiencies of the gradient porous aerogel remained highly stable over 10 consecutive evaporation cycles in a 3.5 wt% NaCl solution. Furthermore, as illustrated in Fig. 5l, the aerogel also maintained nearly constant evaporation rates and solar-to-vapor conversion efficiencies across a wide range of saline concentrations with 3.5, 5, 10, and 20 wt% NaCl. These results are attributed to the synergistic interplay between the vertical gradient channels and embossed surface microstructure, which together promotes directional water transport, suppresses salt accumulation, and enables continuous salt dissolution during operation.

To assess the practical feasibility of the embossed gradient porous aerogel in addressing freshwater scarcity, a field-scale outdoor evaporation and condensate collection system was constructed, as illustrated in Fig. 6a–c and Fig. S22. During field testing, the solar irradiance peaked at approximately 86.27 mW cm^{-2} around 15:00 (Fig. 6d), aligning with the observed internal temperature variation within the system. Throughout the measurement period, the system achieved a high pure water collection rate of 1.65 mL m^{-2} h^{-1}, demonstrating effective solar-driven water vapor generation and condensation capability of the aerogel under natural sunlight. As shown in Fig. 6e, the ambient humidity reached its lowest value (38%) while the temperature of both the designed structural aerogel and the outside condenser peaked at 40.2 °C and 32.5 °C, respectively, at 13:00. These findings underscore the practical potential of the embossed gradient porous aerogel as a scalable, sustainable and efficient material solution for solar-driven desalination, particularly in real-world, off-grid environments.

3. Conclusion

In summary, we have designed and fabricated a novel floatable CNF-based aerogel featuring a gradient-structured directional porous architecture, serving as a multifunctional platform for photocatalytic H$_2$ production and photothermal steam generation applications. The aerogel integrates multiple structural features, including a bottom layer with large directional channels for rapid water transport, a top functional floatable layer with small directional channels for enhanced gas separation and active material loading, and a micron-scale embossed surface structure to maximize light absorption. This gradient-structured design imparts superior light-harvesting capability, efficient water transportation, and effective gas separation, enabling outstanding solar-driven performance compared with single-structure counterparts, such as those with only large channels or lacking the embossed surface. As a result, the photocatalytic aerogels achieved a high hydrogen generation rate of 60.7 mmol m^{-2} h^{-1}, significantly outperforming the conventional thin-film photocatalytic platforms. Meanwhile,

the photothermal aerogels exhibited a high water evaporation rate of 1.62 kg m^{-2} h^{-1} with excellent salt-resistance capability, and a rapid freshwater collection rate of 1.65 mL m^{-2} h^{-1} in an outdoor field-scale evaporation and condensate collection system. This multifunctional, gradient-structured floatable aerogel provides new insights and simple methodologies for the development of efficient solar-driven reaction platforms and holds great promise for future industrial-scale applications.

4. Materials and methods

4.1 Fabrication of the gradient-structured directional porous floatable aerogels

The gradient-structured aerogels were fabricated *via* sequential directional freezing of two different concentrations of CNF solutions. The bottom layer, designed to form large channels, was prepared using a 0.5 wt% CNF solution. The top layer, used to create small channels, was prepared with a 1.0 wt% CNF solution and patterned with a micrometer-imprinted embossed structure using a 3D-printed mold. Specifically, the 0.5 wt% CNF solution was first poured into a polypropylene mold (∅38 × 20 mm) and frozen under liquid nitrogen. After solidifying the bottom layer, the 1.0 wt% CNF solution was carefully added on top. A 3D-printed mold was then applied to the surface of the top layer to imprint the micron-scale pattern. The full fabrication process was carried out under liquid nitrogen freezing to establish a vertical temperature gradient. Finally, the entire structure was subjected to freeze-drying for 24 hours. For comparison, the monolayer and other multilayer aerogel structures were prepared using the same method and used as control samples.

4.2 Preparation of the CTF-BIP photocatalyst

The CTF-BIP photocatalyst was synthesized following the procedure established in our previous study.[56] Specifically, [1,1′-biphenyl]-4,4′-dicarbaldehyde (BIP) (0.5 mmol, 67.6 mg), terephthalimidamide dihydrochloride (1.0 mmol, 235.2 mg), and cesium carbonate (2.2 mmol, 716.8 mg) were added to a 50 mL round-bottom flask containing a mixed solution consisting of dimethyl sulfoxide (DMSO, 5.0 mL) and water (0.2 mL). The reaction mixture was stirred and heated at 120 °C for 72 h, yielding a yellow solid. The resulting precipitate was sequentially washed with dilute hydrochloric acid, water, and acetone to remove unreacted residues and by-products. It was then dried under vacuum at 65 °C for 12 h to obtain the final CTF-BIP product in yellow powder form. To prepare the functional layer for solar-driven hydrogen evolution, a certain amount of CTF-BIP powder was homogeneously mixed well with the top-layer CNF solution using a high-speed homogenizing mixer.

4.3 Preparation of the MXene/r-GO photothermal material

A defined amount of MXene and r-GO was dispersed in 40 mL of deionized water and sonicated for 2 h to ensure uniform dispersion. The resulting suspensions were stirred overnight on a magnetic stirrer to achieve a homogeneous and

stable solution. The mixtures were then subjected to centrifugal separation to collect the black solid precipitates, which were subsequently dried under vacuum at 65 °C for 12 h. The final MXene/r-GO product was obtained as black-brown fine powders. Following the same procedure as for the preparation of the CTF-BIP/CNF functional layer, the photothermal MXene/r-GO material was uniformly mixed with the top-layer CNF solution.

4.4 Material characterization

The micro-morphological features of the samples were examined using a field emission scanning electron microscope (SEM, FEI Inspect F50). The materials were characterized using X-ray diffraction with Cu Kα radiation ($\lambda = 1.5418$ Å) (XRD, Rigaku Smartlab 3). The compressive mechanical properties were measured using a mechanical testing machine (Instron 5848) equipped with a 500 N load cell, operated at a constant compression speed of 3 mm min^{-1}. Micron-scale embossed pattern designs were created using Cinema 4D software and fabricated *via* a light-curing 3D printer (model DJ89 Pro). Thermogravimetric analysis (TGA) was conducted using a thermal analyzer (Netzsch, TG209 F3) at a heating rate of 10 °C min^{-1} under a nitrogen atmosphere. UV-visible diffuse reflectance spectra were recorded using a UV-vis spectrophotometer (Shimadzu UV-3600i Plus dual-beam). Surface temperature distribution and photothermal performance of the aerogels were assessed using an infrared thermographic camera (MDL-N-808-10 W, Changchun New Industry Optoelectronic Technology). All digital photographs of the samples were captured using a Nikon Z30 digital camera.

4.5 COMSOL multiphysics simulation

Water transport in aerogels with disordered, large, and small channel structures was simulated using COMSOL Multiphysics (Fig. S23). The pre-processing steps for the simulation included model construction, fluid domain definition, selection of an appropriate flow field mathematical model, and mesh generation. First, 3D geometric models representing the three structures were constructed using a professional modeling software. Considering the porous nature and micrometer-scale channels of the aerogels, viscous shear effects were deemed significant. Therefore, the Brinkman equation,[68] available under the Porous Media Flow module in COMSOL, was selected as the governing equation. The equation takes the following form:

$$\nabla p = \mu \nabla^2 u - \frac{\mu}{\chi} u,$$

where μ is the fluid viscosity, χ represents the permeability of the porous medium.

The permeability was estimated using the Kozeny–Carman equation:[69]

$$\chi = \frac{\phi^3 d_{\mathrm{p}}^2}{1801 - \phi^2}$$

where ϕ is the porosity and d_{p} is the particle diameter.

Boundary conditions were set with an inlet pressure of 1.0 Pa, an outlet pressure of 0 Pa, and all other surfaces defined as inner walls of the flow field. Liquid water was selected as the working fluid. For the mesh, a regular resolution was applied, generated *via* the physics-controlled mesh option in COMSOL. This choice was made to strike a balance between computational efficiency and simulation accuracy, given that the objective was to evaluate the overall flow velocity field rather than examine localized flow details.

4.6 Photocatalytic hydrogen production test

Photocatalytic hydrogen evolution experiments were conducted following established procedures. A 300 W xenon lamp equipped with an AM 1.5G filter was used as the light source. The actual light intensity at the sample surface was calibrated to 100 ± 5 mW cm^{-2} using a spectroradiometer (CEL-NP2000, CEAULIGHT), and the spectral distribution was confirmed to match the AM 1.5G standard (Fig. S24). Prior to testing, Pt (3.0 wt%) was loaded onto 10 mg of the photocatalyst *via in situ* photo-deposition. The photocatalyst was then dispersed in a mixed solution containing 27 mL of deionized water and 3 mL of triethanolamine (TEOA) as a sacrificial reagent. During the reaction, the temperature was maintained at 25 °C using a circulating water cooling system. The evolved hydrogen was quantified using a gas chromatograph (Agilent, GC-7890B) equipped with a thermal conductivity detector (TCD), with Ar as the carrier gas. Each measurement was repeated at least three times, and the average value was reported to ensure accuracy and reproducibility.

4.7 Photoelectrochemical measurements

Photoelectrochemical measurements were conducted according to established procedures using an electrochemical workstation (Bio-Logic) equipped with a standard three-electrode system. A platinum plate electrode and an Ag/AgCl electrode were used as a counter electrode and reference electrode, respectively. The working electrode was immersed in a 0.5 M Na$_2$SO$_4$ solution as the electrolyte. Photocurrent response tests were carried out under periodic on/off light irradiation to evaluate the charge separation and transfer behavior of the photocatalytic materials.

4.8 Photothermal steam generation test

Photothermal steam generation performance was evaluated under controlled laboratory conditions of 25 °C and 30% relative humidity using a solar simulator (CME-SL500, Micronergy) equipped with an AM1.5G filter and adjustable optics. The solar irradiance was calibrated to 1000 W m^{-2} using a power meter (TES-123). The aerogel-based evaporator was floated on the surface of the water. Water mass loss due to evaporation was monitored in real-time using a precision laboratory balance (BCE224-1CCN, Sartorius).

Notably, all photothermal conversion efficiency could be calculated using the following equation:[70]

$$\eta = m \cdot h_{\mathrm{lv}} / (3600 \cdot q \cdot C_{\mathrm{opt}})$$

where m is the mass of water evaporated per unit area per hour (kg); q denotes the standardized solar radiation (1 kW m^{-2}); C_{opt} represents the optical concentration factor; h_{lv} denotes the

total enthalpy of the liquid phase (kJ kg^{-1}), calculated as $h_{lv} = \lambda + C \cdot \Delta T$. Here, λ represents the latent heat of phase change (kJ kg^{-1}), calculated as $\lambda = 1.91846 \times 10^3 \times (T/(T - 33.91))^2$, where T is the final surface temperature (K). C stands for the specific heat capacity of water (4.2 kJ kg^{-1} K^{-1}), and ΔT is the change in water temperature (K).

Author contributions

Changsong Shi: writing – original draft, validation, methodology, investigation, formal analysis, data curation. Rongtao Zheng: photothermal evaporation experiment. Yihe Yue: finite element analysis. Mingliang Wu: validation, formal analysis. Pengfei Li: investigation. Linfeng Fan: conceptualization, investigation. Chi Guo: methodology. Xin Zhang: methodology. Peiyu Luo: methodology. Li Xiang: resources. Cuilian Wen: supervision. Jinlan Wang: supervision. writing – review & editing, funding acquisition, project management. Baisheng Sa: writing – review & editing, supervision, funding acquisition. Zhiyang Lyu: conceptualization, writing – review & editing, supervision, funding acquisition, project management.

Conflicts of interest

The authors declare no conflict of interest.

Data availability

The data supporting the findings of this study are provided within the article and its SI. Supplementary information: Additional experimental preparation schemes, material characterization data (XRD, TG, SEM, UV–Vis), photocatalysis and photothermal evaporation results, and the COMSOL simulation model (PDF). See DOI: **https://doi.org/10.1039/d5nh00359h**

Acknowledgements

References

1 S. Wan, W. Wang, B. Cheng, G. Luo, Q. Shen, J. Yu, J. Zhang, S. Cao and L. Zhang, *Nat. Commun.*, 2024, **15**, 9612.

2 S. Hu, M.-L. Gao, J. Huang, H. Wang, Q. Wang, W. Yang, Z. Sun, X. Zheng and H.-L. Jiang, *J. Am. Chem. Soc.*, 2024, **146**, 20391–20400.

3 B. Chen, A. Mansouri, C. M. Rueda-Navarro, I. Dovgaliuk, P. Boullay, A. Melillo, J. J. Ramírez-Hernández, B. Xiao, D. Fan, L. A. Fernando, G. Patriarche, I. Cornu, P. Florian, G. Maurin, S. Navalón, H. Garcia, G. Mouchaham and C. Serre, *Adv. Energy Mater.*, 2025, 2500211.

4 B. Yang, Z. Zhang, P. Liu, X. Fu, J. Wang, Y. Cao, R. Tang, X. Du, W. Chen, S. Li, H. Yan, Z. Li, X. Zhao, G. Qin, X.-Q. Chen and L. Zuo, *Nature*, 2023, **622**, 499–506.

5 A. Hu, Y. Zhao, Q. Hu, C. Chen, X. Lu, S. Cui and B. Liu, *Nat. Commun.*, 2024, **15**, 9484.

6 Y. Chen, L. Shen, Z. Qi, Z. Luo, X. Li and H. Bao, *Nat. Sustainability*, 2025, **8**, 162–169.

7 C.-C. Wang, J.-R. Li, X.-L. Lv, Y.-Q. Zhang and G. Guo, *Energy Environ. Sci.*, 2014, **7**, 2831–2867.

8 T. Lu, Y. Zhang, Z. Wang, S. Li, L. Zheng and H. Li, *Nano Energy*, 2024, **127**, 109712.

9 J. Zhang, X. Hou, K. Zhang, Q. Xiao, J. L. Gardea-Torresdey, X. Zhou and B. Yan, *Water Res.*, 2025, **269**, 122802.

10 M. Dan, S. Yu, W. Lin, M. Abdellah, Z. Guo, Z. Q. Liu, T. Pullerits, K. Zheng and Y. Zhou, *Adv. Mater.*, 2025, **37**, e2415138.

11 L. Hou, S. Li, Y. Qi, J. Liu, Z. Cui, X. Liu, Y. Zhang, N. Wang and Y. Zhao, *ACS Nano*, 2025, **19**, 9636–9683.

12 W. K. Chong, B. J. Ng, L. L. Tan and S. P. Chai, *Chem. Soc. Rev.*, 2024, **53**, 10080–10146.

13 B. A. Pinaud, J. D. Benck, L. C. Seitz, A. J. Forman, Z. Chen, T. G. Deutsch, B. D. James, K. N. Baum, G. N. Baum, S. Ardo, H. Wang, E. Miller and T. F. Jaramillo, *Energy Environ. Sci.*, 2013, **6**, 1983–2002.

14 A. Annamalai, S. Sangaraju and S. Elumalai, *Coord. Chem. Rev.*, 2025, **535**, 216646.

15 H. Pan, J. Li, Y. Wang, Q. Xia, L. Qiu and B. Zhou, *Adv. Sci.*, 2024, **11**, e2402651.

16 H. Hu, X. Li, K. Zhang, G. Yan, W. Kong, A. Qin, Y. Ma, A. Li, K. Wang, H. Huang, X. Sun and T. Ma, *Adv. Mater.*, 2025, **37**, 2419023.

17 J. Bi, C. Li, J. Ren, Y. Zhao, Z. Ji, T. Wang, X. Huang and H. Hao, *Adv. Funct. Mater.*, 2024, **34**, 2407834.

18 Y. Chen, L. Soler, C. Cazorla, J. Oliveras, N. G. Bastus, V. F. Puntes and J. Llorca, *Nat. Commun.*, 2023, **14**, 6165.

19 Y. Xu, F. Qiu, S. Q. Xu, S. Zhu, Y. Zhang, H. Liu, P. Zong, L. Ma, K. Hong and Y. Wang, *Adv. Funct. Mater.*, 2024, **35**, 2417553.

20 K. Yang, Y. Huang, T. Wang, Y. Li, Y. Du, J. Ling, Z. Fan, C. Zhang and C. Ma, *Adv. Mater.*, 2024, **36**, e2409832.

21 H. Huang, Z. Chen, Y. Yang, Y. Lin, Y. Fan, X. Wu, Y. Ji, Y. Wang, C. Yang, Y. Yu and Z. Zou, *Adv. Funct. Mater.*, 2024, **35**, 2414298.

22 X. Wang, X. Sui, M. Wang, Z. Zheng, H. Yuan, S. Yang, H. G. Yang, Y. Peng and Y. Hou, *Appl. Catal., B*, 2025, **365**, 124937.

23 H. Zhang, W. Wei, K. Chi, Y. Zheng, X. Y. Kong, L. Ye, Y. Zhao and K. A. I. Zhang, *ACS Catal.*, 2024, **14**, 17654–17663.

24 P. Xiong, S. Zhang, R. Wang, L. Zhang, Q. Ma, X. Ren, Y. Gao, Z. Wang, Z. Guo and C. Zhang, *Energy Environ. Sci.*, 2023, **16**, 3181–3213.

25 N. Lazaar, S. Wu, S. Qin, A. Hamrouni, B. Bikash Sarma, D. E. Doronkin, N. Denisov, H. Lachheb and P. Schmuki, *Angew. Chem., Int. Ed.*, 2025, **64**, e202416453.

26 N. Panangattu Dharmarajan, M. Fawaz, C. I. Sathish, S. N. Talapaneni, K. Ramadass, A. M. Sadanandan, X. M. C. Ta,

M. Huš, V. Perumalsamy, A. Tricoli, B. Likozar, C. H. Jeon, J. H. Yang and A. Vinu, *Adv. Energy Mater.*, 2024, **14**, 2400686.

27 Z. Xing, J. Zhang, J. Cui, J. Yin, T. Zhao, J. Kuang, Z. Xiu, N. Wan and W. Zhou, *Appl. Catal., B*, 2018, **225**, 452–467.

28 X. Liu, J. Pan, H. Huang, X. Zhang, N. Sun, C. Gu, Y. Zhuang and L. Wang, *Chem. Eng. J.*, 2023, **476**, 146868.

29 S. Liu, M. Wang, Y. He, Q. Cheng, T. Qian and C. Yan, *Coord. Chem. Rev.*, 2023, **475**, 214882.

30 Q. Wang, T. Hisatomi, Q. Jia, H. Tokudome, M. Zhong, C. Wang, Z. Pan, T. Takata, M. Nakabayashi, N. Shibata, Y. Li, I. D. Sharp, A. Kudo, T. Yamada and K. Domen, *Nat. Mater.*, 2016, **15**, 611–615.

31 C. S. Gopinath and N. Nalajala, *J. Mater. Chem. A*, 2021, **9**, 1353–1371.

32 N. Nalajala, K. K. Patra, P. A. Bharad and C. S. Gopinath, *RSC Adv.*, 2019, **9**, 6094–6100.

33 Y. Goto, T. Hisatomi, Q. Wang, T. Higashi, K. Ishikiriyama, T. Maeda, Y. Sakata, S. Okunaka, H. Tokudome, M. Katayama, S. Akiyama, H. Nishiyama, Y. Inoue, T. Takewaki, T. Setoyama, T. Minegishi, T. Takata, T. Yamada and K. Domen, *Joule*, 2018, **2**, 509–520.

34 H. Maleki and N. Hüsing, *Appl. Catal., B*, 2018, **221**, 530–555.

35 W. Wan, R. Zhang, M. Ma and Y. Zhou, *J. Mater. Chem. A*, 2018, **6**, 754–775.

36 J. Li, M. Li, C. Guo, X. Zhou, J. Zhang, J. Wang, Y. Chen and Z. Lyu, *Energy Storage Mater.*, 2025, **74**, 103958.

37 Y. Li, X. Ni, S. Zhu, J. Li, C. Guo, M. Li, J. Gong, X. Zhou, J. Lang, Q. Gao, J. Zhang, Y. Chen and Z. Lyu, *Fundam. Res*, 2025, DOI: 10.1016/j.fmre.2025.01.010.

38 Y. Mao, Y. Sheng, Z. Fan, J. Yang, J. Liu, C. Tang and S. Fu, *Adv. Funct. Mater.*, 2025, 2421492.

39 W. Yang, S. Liu, Z. Wang, H. Liu, C. Pan, C. Liu and C. Shen, *Nano Energy*, 2024, **127**, 109799.

40 M. Zhang, S. Liu, S. Liu, G. Jia, P. Zhan, C. Liu, C. Shen and H. Liu, *Adv. Compos. Hybrid Mater.*, 2024, **8**, 79.

41 W. Yang, H. Liu, H. Du, M. Zhang, C. Wang, R. Yin, C. Pan, C. Liu and C. Shen, *Sci. China Mater.*, 2023, **66**, 2829–2842.

42 S. Qi, T. Jia, Y. Zhang, Y. Zhao, Y. Xing, M. Zhang, F. Wang, C. Chen and W. Y. Wong, *Adv. Funct. Mater.*, 2025, 2503234.

43 Y. Lu, D. Fan, Y. Wang, H. Xu, C. Lu and X. Yang, *ACS Nano*, 2021, **15**, 10366–10376.

44 J. Ma, X. Sun, Y. liu, L. Wang, M. An, M. Kim, Y. Yamauchi, N. Khaorapapong and Z. Yuan, *Nano Energy*, 2025, **137**, 110781.

45 T. Wang, M. Li, H. Xu, X. Wang, M. Jia, X. Hou, S. Gao, Q. Liu, Q. Yang, M. Tian, L. Qu, Z. Song, X. Wu, L. Wang and X. Zhang, *Nano-Micro Lett.*, 2024, **16**, 220.

46 X. An, T. Li, J. Chen and D. Fu, *Energy*, 2023, **274**, 127392.

47 W. Zhu, M. Chen, J. Jang, M. Han, Y. Moon, J. Kim, J. You, S. Li, T. Park and J. Kim, *Carbohydr. Polym.*, 2024, **323**, 121393.

48 C. Wang, Y. Wang, M. Yan, W. Zhang, P. Wang, W. Guan, S. Zhang, L. Yu, J. Feng, Z. Gan and L. Dong, *J. Colloid Interface Sci.*, 2023, **630**, 297–305.

49 L. Ying, F. Liang, Z. Huang, J. Ding, W. Wang, S. Liu and J. Lu, *Chem. Eng. J.*, 2023, **474**, 145709.

50 C. Cai, Y. Chen, F. Cheng, Z. Wei, W. Zhou and Y. Fu, *ACS Nano*, 2024, **18**, 4376–4387.

51 H. Ghasemi, G. Ni, A. M. Marconnet, J. Loomis, S. Yerci, N. Miljkovic and G. Chen, *Nat. Commun.*, 2014, **5**, 5449.

52 A. Javadi, Q. Zheng, F. Payen, A. Javadi, Y. Altin, Z. Cai, R. Sabo and S. Gong, *ACS Appl. Mater. Interfaces*, 2013, **5**, 5969–5975.

53 S. Wei, Y. C. Ching and C. H. Chuah, *Carbohydr. Polym.*, 2020, **231**, 115744.

54 T. Zhu, D. Wang, Y. Wang, F. Xu, J. Huang, M. Lian, Y. Wang, W. Fan, Y. E. Miao, J. Zhu, D. H. Nguyen, C. Zhang and T. Liu, *Adv. Funct. Mater.*, 2025, 2503693.

55 X. Long, J. Qin, J. Tang, J. Xue, Y. Wang, L. Zhou, S. Wang, X. Wei, Y. Lin and J. Liao, *Adv. Funct. Mater.*, 2024, **35**, 2413018.

56 M. Wu, Z. Song, Y. Cui, Z. Fu, K. Hong, Q. Li, Z. Lyu, W. Liu and J. Wang, *Adv. Funct. Mater.*, 2024, **35**, 2413453.

57 M. Wu, J. Sun, Y. Cui, L. Fan, K. Hong, W. Liu, Q. Li, Z. Lyu and J. Wang, *Adv. Funct. Mater.*, 2025, 2505234.

58 L. P. Rao Pala and N. R. Peela, *Energy Fuels*, 2021, **35**, 19737–19747.

59 D. J. Woods, S. A. J. Hillman, D. Pearce, L. Wilbraham, L. Q. Flagg, W. Duffy, I. McCulloch, J. R. Durrant, A. A. Y. Guilbert, M. A. Zwijnenburg, R. S. Sprick, J. Nelson and A. I. Cooper, *Energy Environ. Sci.*, 2020, **13**, 1843–1855.

60 X. Wang, L. Chen, S. Y. Chong, M. A. Little, Y. Wu, W. H. Zhu, R. Clowes, Y. Yan, M. A. Zwijnenburg, R. S. Sprick and A. I. Cooper, *Nat. Chem.*, 2018, **10**, 1180–1189.

61 X. Hu, Z. Zhan, J. Zhang, I. Hussain and B. Tan, *Nat. Commun.*, 2021, **12**, 6596.

62 G. Wei, F. Niu, Z. Wang, X. Liu, S. Feng, K. Hu, X. Gong and J. Hua, *Mater. Today Chem.*, 2022, **26**, 101075.

63 W. H. Lee, C. W. Lee, G. D. Cha, B.-H. Lee, J. H. Jeong, H. Park, J. Heo, M. S. Bootharaju, S.-H. Sunwoo, J. H. Kim, K. H. Ahn, D.-H. Kim and T. Hyeon, *Nat. Nanotechnol.*, 2023, **18**, 754–762.

64 L. He, X. Zeng, H. Chen, L. Zhao, Z. Huang, D. Wang, X. He, W. Fang, X. Du and W. Li, *Adv. Funct. Mater.*, 2024, **34**, 2313058.

65 N. Ma, L. Dong, T. Zhang, N. e Xie, L. Tian, Z. Zhang, X. Guan and L. Guo, *J. Colloid Interface Sci.*, 2025, **687**, 573–581.

66 C. Wen, X. Li, S. Yan, J. Wen, R. Zheng, X. Wang, H. Zhao, J. Zhou, B. Sa and Z. Sun, *Chem. Eng. J.*, 2025, **510**, 161873.

67 Y. Shao, A. Shen, N. Li, L. Yang, J. Tang, H. Zhi, D. Wang and G. Xue, *ACS Appl. Mater. Interfaces*, 2022, **14**, 30324–30331.

68 S. K. Zaripov, R. F. Mardanov and V. F. Sharafutdinov, *Transp. Porous Media*, 2019, **130**, 529–557.

69 M. Rehman, M. B. Hafeez and M. Krawczuk, *Arch. Comput. Methods Eng.*, 2024, **31**, 3843–3855.

70 M. Ye, X. Ye, X. Zhou, Y. Yan, T. Zhang and X. Liu, *J. Environ. Chem. Eng.*, 2024, **12**, 114680.